

Title: Quantum state resolution of the C₆₀ fullerene

Authors: P. Bryan Changala^{1*}, Marissa L. Weichman¹, Kevin F. Lee², Martin E. Fermann², Jun Ye^{1*}

Affiliations:

¹JILA, National Institute of Standards and Technology and University of Colorado, Department of Physics, University of Colorado, Boulder, Colorado 80309, USA.

²TMRA America, Inc., 1044 Woodridge Ave., Ann Arbor, Michigan 48105, USA.

*Corresponding authors: bryan.changala@colorado.edu (P.B.C.), ye@jila.colorado.edu (J.Y.)

Abstract: The remarkable physical properties of buckminsterfullerene, C₆₀, have attracted intense research activity since its original discovery. Total quantum state resolved measurements of isolated C₆₀ molecules have been of particularly long-standing interest. However, such observations have to date been unsuccessful due to the difficulty in preparing cold, gas-phase C₆₀ in sufficiently high densities. Here we report high resolution infrared absorption spectroscopy of C₆₀ in the 8.5 μm spectral region. A combination of cryogenic buffer gas cooling and cavity-enhanced direct frequency comb spectroscopy has enabled the observation of quantum state resolved rovibrational transitions. Characteristic nuclear spin statistical intensity patterns provide striking confirmation of the indistinguishability of the sixty ¹²C atoms, while rovibrational fine structure encodes further details of the molecule's rare icosahedral symmetry. These observations establish new possibilities in the study and control of emergent complexity in finite-sized quantum systems such as fullerenes.

One Sentence Summary: High resolution infrared spectroscopy of cold, gas-phase C₆₀ reveals fundamental details of its quantum mechanical structure.

Main Text:

Understanding molecules as quantum mechanical systems is a central objective of chemical and molecular physics. The complex internal dynamics of these systems evolve over wide energy and time scales as exhibited by the various electronic, vibrational, rotational, and spin degrees of freedom. Polyatomic molecules, in particular, offer the prospect of probing many-body physics in strongly interacting systems. The most comprehensive characterization of a molecular Hamiltonian, which governs intramolecular dynamics, is provided with high resolution spectroscopy. When a polyatomic molecule is sufficiently cold to concentrate the population into and thereby spectrally probe a single rovibrational state, we achieve the unimolecular equivalent of a pure quantum state at absolute zero in the rest frame of the molecule. The precise measurement of transition energies between individual molecular eigenstates yields detailed information about strong, multi-body interactions between atoms in a unimolecular polyatomic lattice, thus providing profound insights into complex molecular structure and ensuing interaction dynamics.

Here we report the first rotationally resolved spectrum of buckminsterfullerene, C₆₀. Following the discovery of C₆₀ by Kroto *et al.* in 1985 (1), infrared and ¹³C NMR spectroscopy confirmed its caged, icosahedral structure (2-7). Subsequent spectroscopic and analytical

techniques, including x-ray and electron diffraction (8, 9), optical Raman and neutron scattering (10-15), matrix isolation infrared spectroscopy (see (16-18) and references therein), and photoelectron spectroscopy (19, 20), have greatly advanced our understanding of this remarkable molecule. Spectroscopy has also played a central role in the astronomical detection of C₆₀ and its derivatives (21, 22). However, to date, there have been no reports of total quantum state resolved measurements of isolated gas-phase C₆₀ molecules. The experiments reported here thus establish C₆₀ as the largest molecule, and the only example of rare icosahedral symmetry, for which a complete internal quantum state resolved spectrum has been observed.

While quantum state resolved spectroscopy is routine for small, light molecules, systems as large and heavy as C₆₀ are much less amenable to high resolution characterization. Rovibrational spectroscopy in the infrared region is made especially difficult due to several intrinsic and technical challenges. The increase in both the number of vibrational modes and the magnitude of the moment of inertia for every additional atom results in significantly more rotation-vibration states populated at a given internal temperature. Rovibrational states excited by an infrared photon may be strongly coupled to a highly congested manifold of background dark states, the density of which grows rapidly with increasing internal energy, leading to intramolecular vibrational redistribution (23). The Doppler broadening of optical transitions due to finite translational temperature serves only to exacerbate this spectral congestion. Furthermore, the low gas-phase densities achievable for heavy, non-volatile species require high detection sensitivity.

These various experimental challenges are addressed by cooling the translational and internal temperatures of gas-phase molecular samples. The method of cryogenic buffer gas cooling is particularly effective for large, heavy molecules (24, 25). We have recently demonstrated the integration of a buffer gas cooling source with cavity-enhanced direct frequency comb spectroscopy (CE-DFCS) in the mid-infrared (26, 27), which enables sensitive, broadband, high resolution absorption measurements (28, 29). We have since extended this apparatus to the long-wave infrared (LWIR) region (30) and made significant changes to the buffer gas cooling conditions to permit the preparation and detection of cold, gas-phase samples of even heavier molecules.

Figure 1A depicts a simplified view of the apparatus used for C₆₀ cooling and spectroscopy. A 950 K copper oven sublimates solid C₆₀ samples, generating gas-phase C₆₀ with an average internal energy of 6-8 eV per molecule and occupying up to an estimated 10²⁶-10³⁰ vibrational quantum states, as shown in Fig. 1B. These hot molecules flow into a cell anchored to a cryogenic cold finger, where they are thermalized close to the cell wall temperature via collisions with cold buffer gas atoms introduced through an annular slit inlet plate surrounding the cell entrance aperture. We interrogate the cold gas-phase molecules with CE-DFCS by coupling a frequency comb into a high finesse optical cavity surrounding the cold cell, which enhances the absorption signal by a factor on the order of the cavity finesse ($F = 6000$). The LWIR frequency comb light centered near 8.5 μm is produced by difference frequency generation (DFG) with two near-infrared frequency combs originating from a single mode-locked fiber laser (31). The comb contains narrow “teeth” at optical frequencies $\nu_m = m \times f_{\text{rep}} + f_0$, where f_{rep} is the repetition rate. While the DFG comb does not have an offset frequency f_0 , it can be introduced via an external acousto-optic modulator before the difference frequency step. The intensity of each comb tooth transmitted through the cavity is read out using a broadband scanning-arm Fourier transform interferometer (32, 33). Additional experimental details are provided in Materials and Methods (34).

Our first attempts at observing cold gas-phase C_{60} with low pressure helium buffer gas conditions similar to our previous work (26, 27) yielded no detectable absorption. However, when the vacuum chamber was flooded with a high pressure of helium buffer gas, a single broad, unresolved absorption feature appeared, as shown by the red trace in Fig. 2A. We attribute this spectrum to partially cooled C_{60} molecules that remain warm enough to occupy many vibrational quantum states. This is not surprising: as can be seen in Fig. 1B, even at room temperature the vibrational partition function is greater than 10^3 . This finding suggested that both a higher number of collisions and more efficient energy transfer per collision would be required to thermalize C_{60} to its ground vibrational state (35). Indeed, we ultimately produced a sufficiently dense, cold C_{60} sample by (i) increasing the buffer gas mass by switching from helium to argon and (ii) carefully optimizing the buffer gas flow and oven positioning relative to the inlet slit. The spectrum acquired at these conditions is shown by the blue trace in Fig. 2A and exhibits well resolved rovibrational fine structure, with narrow linewidths on the order of 20 MHz (Fig. S1). The peak absorption, near the band origin, is 10% of the cavity-transmitted comb mode intensity. From the magnitude of the integrated absorption cross-section (17), we estimate the number density of cold C_{60} to be $4 \times 10^{11} \text{ cm}^{-3}$. Observing the appearance and evolution between the broad and narrow signals was greatly facilitated by the wide spectral bandwidth of the frequency comb, which covers the entire breadth of the observed vibrational band. The inferred rotational temperature is approximately 150 K (34), nearly equal to the cell wall temperature of 135 K, which is kept well above argon’s condensation point of 87 K.

The observed fine structure in the infrared spectrum encodes fundamental details of the quantum mechanical structure of C_{60} . To zeroth order, the rotations of C_{60} can be considered as those of a spherical top with total angular momentum operator \mathbf{J} (36). The associated rotational quantum states are $|J, k, m\rangle$, where $J = 0, 1, 2, \dots$ is the total angular momentum quantum number, and $k, m = -J, \dots, +J$ are the projection quantum numbers of the body-fixed component (J_z) and lab-fixed component (J_Z) of \mathbf{J} , respectively. The triply degenerate vibrational mode of T_{1u} symmetry that gives rise to the infrared band can be modeled as a 3D isotropic harmonic oscillator with vibrational angular momentum operator ℓ . Its quantum states are $|n, \ell, k_\ell\rangle$, where n is the total number of vibrational quanta, $\ell = n, n-2, n-4, \dots$ is the vibrational angular momentum quantum number, and $k_\ell = -\ell, \dots, +\ell$ is the projection quantum number of the body-frame projection (ℓ_z) of ℓ .

The uncoupled rovibrational product wavefunctions $|J, k, m\rangle|n, \ell, k_\ell\rangle$ are simultaneously eigenfunctions of \mathbf{J}^2 , ℓ^2 , J_z , ℓ_z and J_Z . It is useful to define the “pure rotational” angular momentum $\mathbf{R} = \mathbf{J} - \ell$, the eigenfunctions of which can be constructed by transforming the uncoupled product wavefunctions using standard angular momentum coupling relations (36). This yields total coupled rovibrational wavefunctions of the form $|R, k_R, J, \ell, n, m\rangle$, where R is the angular momentum quantum number of \mathbf{R} and $k_R = -R, \dots, +R$ is the body-fixed projection. As usual, the values of R satisfy the triangle inequality $R = |J - \ell|, \dots, J + \ell$. In this work, we are concerned only with the ground vibrational state with $n = \ell = 0$ and the excited T_{1u} vibrational

state, populated by the IR photon, with $n = \ell = 1$. Therefore, in the ground vibrational state, $R = J$; similarly, in the excited state where $\ell = 1$, R is restricted to $J, |J \pm 1|$.

The energies of the states we observe are determined by effective rotational Hamiltonians for each vibrational state. The simplest possible effective Hamiltonian for the ground vibrational state is that of a rigid spherical top

$$H_{gr} = B'' \mathbf{J}^2, \quad (1)$$

where B'' is the ground state rotational constant, which is inversely proportional to the moment of inertia. The ground state wavefunctions $|R = J, k_R, J, \ell = 0, n = 0, m\rangle$ are eigenstates of H_{gr} with energies

$$E_{gr} = B'' J(J + 1). \quad (2)$$

This energy is independent of k_R and m , leading to the usual $(2R + 1)(2J + 1) = (2J + 1)^2$ spherical top ground state degeneracy factor.

The excited vibrational state is described to lowest order by a slightly more sophisticated effective Hamiltonian,

$$H_{ex} = v_0 + B' \mathbf{J}^2 - 2B'\zeta(\mathbf{J} \cdot \boldsymbol{\ell}), \quad (3)$$

where v_0 is the vibrational band origin, and B' is the excited state rotational constant, which differs slightly from B'' due to changes of the moment of inertia upon vibrational excitation. The new rightmost term arises from Coriolis forces that couple the total angular momentum \mathbf{J} and the vibrational angular momentum $\boldsymbol{\ell}$, with $\ell = 1$. The ζ constant encodes the strength of this coupling, which is determined by the geometric details of the vibrational normal mode. The excited state wavefunctions $|R, k_R, J, \ell = 1, n = 1, m\rangle$ are eigenstates of H_{ex} with energy levels at

$$E_{ex} = v_0 + B' J(J + 1) - B'\zeta [J(J + 1) + \ell(\ell + 1) - R(R + 1)], \quad (4)$$

again with a degeneracy of $(2R + 1)(2J + 1)$. As $R = J, |J \pm 1|$, the excited state energies sort into three distinct manifolds (37)

$$\begin{aligned} E_{ex}^{(+)} &= E_J + 2B'\zeta J, & R &= J + 1, \\ E_{ex}^{(0)} &= E_J - 2B'\zeta, & R &= J, \\ E_{ex}^{(-)} &= E_J - 2B'\zeta(J + 1), & R &= J - 1, \end{aligned} \quad (5)$$

where $E_J = v_0 + B' J(J + 1)$ is the pure vibrational and rigid rotor contribution to the energy. Physically, these manifolds correspond to states where \mathbf{J} and $\boldsymbol{\ell}$ are mutually antiparallel, perpendicular, and parallel, respectively.

Rovibrational transitions between the ground and excited T_{1u} vibrational states of spherical tops such as C_{60} are governed by the usual strict $\Delta J = 0, \pm 1$ rule and an additional $\Delta R = \Delta k_R = 0$ rule (36). These allowed transitions are illustrated in the level diagram of Fig. 2B. Unlike less symmetric molecules, these selection rules dictate that the usual P ($\Delta J = -1$), Q ($\Delta J = 0$), and R ($\Delta J = +1$) transitions reach mutually exclusive sets of upper state quantum levels. These three manifolds are labeled $T_{1u}^{(+)}$, $T_{1u}^{(0)}$, and $T_{1u}^{(-)}$ according to the energy expressions in Eq. (5).

Inspection of the level diagram in Fig. 2B shows that states with certain values of R are missing. This is, in fact, an exceptional example of nuclear spin statistics at work. The carbon nuclei in pure $^{12}C_{60}$ are each identical spin-0 bosons, so any permutation of nuclei must leave the total molecular wavefunction unchanged. This imposes the strict condition that only states with a total rovibronic symmetry of A_g (+ parity) or A_u (- parity) in the I_h point group may exist. Group theoretical analysis (38) of the rovibrational wavefunctions shows that this condition is met only with certain linear combinations of k_R states for a given value of R . In fact, only a *single* such linear combination is possible for $R = 0, 6, 10, 12, 15, 16, 18, 20-22$, and $24-28$, with other values of $R < 30$ having no allowed states. (For levels with $R \geq 30$, the number of allowed states is equal to 1 plus the number of states for R minus 30.) The unusual patterns of allowed angular momentum quantum numbers are intimately related to the 2-, 3- and 5-fold symmetry axes of an icosahedron. In the high- R limit, only 1 in 60 states exist due to the drastic effects of these ^{12}C nuclear spin statistics.

Taking the zeroth order energies, selection rules, and spin statistics all together, one is left with the predicted spectrum plotted in black in Fig. 2A. It consists of a sharp Q branch surrounded by P and R branches containing lines evenly spaced by approximately $(B'' + B')(1 - \zeta) \approx 0.0078$ cm^{-1} . The qualitative appearance of the measured R and Q branch regions is consistent with the simulation, while there is substantial disagreement in the P branch. The portions of the spectrum shown in Fig. 3 provide a closer view of this behavior.

The R branch exhibits a regularly spaced progression of transitions $R(J)$ that we have assigned from $J \approx 60-360$. Transitions outside this range are below our detection sensitivity. Such high values of the total angular momentum quantum number have been rarely observed, if ever, by rotationally resolved frequency domain spectroscopy. Portions of the measured and simulated R branch from $J = 160-200$ are shown in Fig. 3A. Despite the noise in the measured absorption, these transitions clearly show the expected discrete intensity variations in the correct integer ratios. Such patterns are a basic consequence of the quantum mechanical indistinguishability and the perfect icosahedral arrangement of the carbon nuclei that make up $^{12}C_{60}$.

Quantitative analysis of the R branch transition frequencies permits extraction of spectroscopic constants. The energy expressions in Eqs. (2) and (5) yield expected transition frequencies of

$$\begin{aligned} \nu[R(J)] = & \nu_0 + (2\bar{B} + \Delta B)(1 - 2\zeta) \\ & + J[2\bar{B}(1 - \zeta) + \Delta B(2 - \zeta)] \\ & + J^2\Delta B, \end{aligned} \quad (6)$$

where $\bar{B} \equiv (B' + B'')/2$ is the mean value of the lower and upper state rotational constants, and $\Delta B \equiv B' - B'' \ll \bar{B}$ is their difference. Figure 4A shows the measured positions (34) as a function of lower state J , which follow the expected nearly linear dependence. Figure 4B shows the

residuals from a fit of Eq. (6) to the measured line positions, displaying two avoided crossings arising from perturbations in the excited state. The fitted spectroscopic parameters are summarized in Table 1. The R branch transition frequencies are well reproduced despite the simplicity of the zeroth order Hamiltonian, which ignores centrifugal distortion effects, and the very high range of J . A complete listing of the approximately three hundred transition frequencies used in this fit is given in Data S1.

These measurements represent the first quantum state resolved gas-phase spectrum reported for C_{60} . As noted by Brieva *et al.* (18) such infrared absorption measurements may help resolve current uncertainties regarding the physical state of astronomical C_{60} . More fundamentally, they provide structural information of isolated gas-phase molecules through the rotational fine structure. While the transitions included in our initial analysis do not yet allow an independent determination of B'' and ζ , if we assume a range of $\zeta = -0.30$ to -0.45 based on theoretical calculations (37) we can estimate $B'' = \frac{1}{hc} \frac{\hbar^2}{2I} \approx 0.0027\text{-}0.0030 \text{ cm}^{-1}$, where I is the effective

moment of inertia of the ground vibrational state. Given $I = \frac{2}{3}mr^2$ for a spherical shell of mass m and radius r , the corresponding range of radii is 3.4 to 3.6 Å. This is consistent with a previous gas-phase electron diffraction measurement of 3.557(5) Å, which includes thermal averaging effects that lengthen the measured radius relative to that of the vibrational ground state (8). Furthermore, our measured value of ΔB implies that the effective C_{60} radius increases by only 0.005% upon excitation of the observed vibrational mode, which is primarily of a surface-tangent C–C bond stretching character. Further analysis of the rotational fine structure of $^{12}C_{60}$ (and ultimately $^{12}C_{59}^{13}C$) will be necessary to constrain B'' and ζ independently and completely determine the gas-phase structural parameters.

The Q branch region is shown in Fig. 3B. There are several unresolved features here, though each is still quite narrow on an absolute scale of 0.01 to 0.03 cm^{-1} . The highest frequency feature is assigned as the Q branch of the $^{12}C_{60}$ isotopologue in its ground vibrational state. Centrifugal distortion effects create a band head observed near $J = 250$ (inset of Fig. 3B). The remaining features in the Q branch region are not definitively assigned. While they are possibly hot band transitions of the $^{12}C_{60}$ isotopologue, we believe they most likely derive from the singly substituted $^{12}C_{59}^{13}C$ isotopologue. Despite a ^{13}C natural abundance of only 1.1%, the sixty equivalent substitution sites lead to a remarkably high ($^{12}C_{59}^{13}C$): $^{12}C_{60}$ ratio of about 2:3. The substitution breaks the icosahedral symmetry of C_{60} , splitting the three-fold degeneracy of the vibrational level and nullifying the nuclear spin statistics. Many more rotational levels and transitions are expected, which will be further split by the non-spherical moments of inertia (39).

Finally, two representative portions of the P branch are shown in Fig. 3C. Here, the zeroth order simulation fails to capture either the position or number of observed transitions. This complicated fine structure is likely due to high order centrifugal distortion terms not included in the simulated spectrum (40). The zeroth order Hamiltonians, Eqs. (1) and (3), contain only scalar terms that preserve the spherical degeneracy of the $(2R+1)$ body-fixed projections of \mathbf{R} . While most of these sub-states are eliminated by the ^{12}C nuclear spin statistics, the degeneracy of the remaining sub-states can be broken by non-scalar centrifugal distortion terms. These so-called “icosahedral splitting” terms (40) lead to subsequent splittings of the observed transitions. In the

ground state, the lowest order non-scalar centrifugal distortion term scales like J^6 , whereas such terms can appear in the excited state that scale only as J^4 . Due to the large J values observed here, it is not surprising that such effects become important. However, to date there have been no theoretical predictions of the magnitude of these icosahedral splitting terms. A full analysis of this portion of the spectrum is most effectively treated within the irreducible spherical tensor formalism (41) and is ongoing in our laboratory.

The present experiments represent the beginning of what we hope is a new avenue of C_{60} research and fullerene science. The general applicability of buffer gas cooling establishes the possibility of similar studies, both in the infrared and other spectral regions, on larger fullerenes such as C_{70} ; endofullerenes, wherein an atom or small molecule is encapsulated in a closed fullerene cage; or even pure $^{13}C_{60}$, which represents a pristine example of a spin- $\frac{1}{2}$ network on a spherical lattice. Ultimately, precision spectroscopy of such targets is the first step towards single quantum state preparation and control of large molecular systems.

References and Notes:

1. H. W. Kroto, J. R. Heath, S. C. O'Brien, R. F. Curl, R. E. Smalley, C_{60} : Buckminsterfullerene. *Nature* **318**, 162-163 (1985).
2. H. Ajie, M. M. Alvarez, S. J. Anz, R. D. Beck, F. Diederich, K. Fostiropoulos, D. R. Huffman, W. Krätschmer, Y. Rubin, K. E. Schriver, D. Sensharma, R. L. Whetten, Characterization of the Soluble All-Carbon Molecules C_{60} and C_{70} . *J. Phys. Chem.* **94**, 8630-8633 (1990).
3. R. Taylor, J. P. Hare, A. K. Abdulsada, H. W. Kroto, Isolation, Separation and Characterization of the Fullerenes C_{60} and C_{70} : the Third Form of Carbon. *J. Chem. Soc., Chem. Commun.* **1990**, 1423-1424 (1990).
4. W. Krätschmer, K. Fostiropoulos, D. R. Huffman, The Infrared and Ultraviolet Absorption Spectra of Laboratory-Produced Carbon Dust: Evidence for the Presence of the C_{60} Molecule. *Chem. Phys. Lett.* **170**, 167-170 (1990).
5. W. Krätschmer, L. D. Lamb, K. Fostiropoulos, D. R. Huffman, Solid C_{60} : a New Form of Carbon. *Nature* **347**, 354-358 (1990).
6. C. S. Yannoni, P. P. Bernier, D. S. Bethune, G. Meijer, J. R. Salem, NMR Determination of the Bond Lengths in C_{60} . *J. Am. Chem. Soc.* **113**, 3190-3192 (1991).
7. C. S. Yannoni, R. D. Johnson, G. Meijer, D. S. Bethune, J. R. Salem, ^{13}C NMR Study of the C_{60} Cluster in the Solid State: Molecular Motion and Carbon Chemical Shift Anisotropy. *J. Phys. Chem.* **95**, 9-10 (1991).
8. K. Hedberg, L. Hedberg, D. S. Bethune, C. A. Brown, H. C. Dorn, R. D. Johnson, M. De Vries, Bond Lengths in Free Molecules of Buckminsterfullerene, C_{60} , from Gas-Phase Electron Diffraction. *Science* **254**, 410-412 (1991).
9. S. Liu, Y.-J. Lu, M. M. Kappes, J. A. Ibers, The Structure of the C_{60} Molecule: X-Ray Crystal Structure Determination of a Twin at 110 K. *Science* **254**, 408-410 (1991).
10. S. F. Parker, S. M. Bennington, J. W. Taylor, H. Herman, I. Silverwood, P. Albers, K. Refson, Complete assignment of the vibrational modes of C_{60} by inelastic neutron scattering spectroscopy and periodic-DFT. *Phys. Chem. Chem. Phys.* **13**, 7789-7804 (2011).

11. L. Pintschovius, Neutron studies of vibrations in fullerenes. *Rep. Prog. Phys.* **59**, 473-510 (1996).
12. D. S. Bethune, G. Meijer, W. C. Tang, H. J. Rosen, The Vibrational Raman Spectra of Purified Solid Films of C₆₀ and C₇₀. *Chem. Phys. Lett.* **174**, 219-222 (1990).
13. D. S. Bethune, G. Meijer, W. C. Tang, H. J. Rosen, W. G. Golden, H. Seki, C. A. Brown, M. S. De Vries, Vibrational Raman and Infrared Spectra of Chromatographically Separated C₆₀ and C₇₀ Fullerene Clusters. *Chem. Phys. Lett.* **179**, 181-186 (1991).
14. K. Prassides, T. J. S. Dennis, J. P. Hare, J. Tomkinson, H. W. Kroto, R. Taylor, D. R. M. Walton, Inelastic Neutron Scattering Spectrum of the Fullerene C₆₀. *Chem. Phys. Lett.* **187**, 455-458 (1991).
15. R. L. Cappelletti, J. R. D. Copley, W. A. Kamitakahara, F. Li, J. S. Lannin, D. Ramage, Neutron Measurements of Intramolecular Vibrational Modes in C₆₀. *Phys. Rev. Lett.* **66**, 3261-3264 (1991).
16. N. Sogoshi, Y. Kato, T. Wakabayashi, T. Momose, S. Tam, M. E. DeRose, M. E. Fajardo, High-resolution infrared absorption spectroscopy of C₆₀ molecules and clusters in parahydrogen solids. *J. Phys. Chem. A* **104**, 3733-3742 (2000).
17. S. Iglesias-Groth, F. Cataldo, A. Manchado, Infrared spectroscopy and integrated molar absorptivity of C₆₀ and C₇₀ fullerenes at extreme temperatures. *Mon. Not. R. Astron. Soc.* **413**, 213-222 (2011).
18. A. C. Brieva, R. Gredel, C. Jäger, F. Huisken, T. Henning, C₆₀ as a Probe for Astrophysical Environments. *Astrophys. J.* **826**, (2016).
19. X.-B. Wang, C.-F. Ding, L.-S. Wang, High resolution photoelectron spectroscopy of C₆₀⁻. *J. Chem. Phys.* **110**, 8217-8220 (1999).
20. D.-L. Huang, P. D. Dau, H.-T. Liu, L.-S. Wang, High-resolution photoelectron imaging of cold C₆₀⁻ anions and accurate determination of the electron affinity of C₆₀. *J. Chem. Phys.* **140**, (2014).
21. J. Cami, J. Bernard-Salas, E. Peeters, S. E. Malek, Detection of C₆₀ and C₇₀ in a Young Planetary Nebula. *Science* **329**, 1180-1182 (2010).
22. E. K. Campbell, M. Holz, D. Gerlich, J. P. Maier, Laboratory confirmation of C₆₀⁺ as the carrier of two diffuse interstellar bands. *Nature* **523**, 322 (2015).
23. D. J. Nesbitt, R. W. Field, Vibrational energy flow in highly excited molecules: Role of intramolecular vibrational redistribution. *J. Phys. Chem.* **100**, 12735-12756 (1996).
24. D. Patterson, E. Tsikata, J. M. Doyle, Cooling and collisions of large gas phase molecules. *Phys. Chem. Chem. Phys.* **12**, 9736-9741 (2010).
25. J. Piskorski, D. Patterson, S. Eibenberger, J. M. Doyle, Cooling, Spectroscopy and Non-Sticking of *trans*-Stilbene and Nile Red. *Chemphyschem* **15**, 3800-3804 (2014).
26. P. B. Changala, B. Spaun, D. Patterson, J. M. Doyle, J. Ye, Sensitivity and resolution in frequency comb spectroscopy of buffer gas cooled polyatomic molecules. *Appl. Phys. B.* **122**, (2016).
27. B. Spaun, P. B. Changala, D. Patterson, B. J. Bjork, O. H. Heckl, J. M. Doyle, J. Ye, Continuous probing of cold complex molecules with infrared frequency comb spectroscopy. *Nature* **533**, 517 (2016).
28. F. Adler, M. J. Thorpe, K. C. Cossel, J. Ye, Cavity-Enhanced Direct Frequency Comb Spectroscopy: Technology and Applications. *Annu. Rev. Anal. Chem.* **3**, 175-205 (2010).
29. M. J. Thorpe, J. Ye, Cavity-enhanced direct frequency comb spectroscopy. *Appl. Phys. B* **91**, 397-414 (2008).

30. K. Iwakuni, G. Porat, T. Q. Bui, B. J. Bjork, S. B. Schoun, O. H. Heckl, M. E. Fermann, J. Ye, Phase-stabilized 100 mW frequency comb near 10 μm . *Appl. Phys. B* **124**, 128 (2018).
31. K. F. Lee, C. J. Hensley, P. G. Schunemann, M. E. Fermann, Midinfrared frequency comb by difference frequency of erbium and thulium fiber lasers in orientation-patterned gallium phosphide. *Opt. Express* **25**, 17411-17416 (2017).
32. J. Mandon, G. Guelachvili, N. Picqué, Fourier transform spectroscopy with a laser frequency comb. *Nat. Photonics* **3**, 99-102 (2009).
33. F. Adler, P. Masłowski, A. Foltynowicz, K. C. Cossel, T. C. Briles, I. Hartl, J. Ye, Mid-infrared Fourier transform spectroscopy with a broadband frequency comb. *Opt. Express* **18**, 21861-21872 (2010).
34. See supplementary material.
35. J. T. Stewart, B. E. Brumfield, B. M. Gibson, B. J. McCall, Inefficient Vibrational Cooling of C_{60} in a Supersonic Expansion. *ISRN Phys. Chem.* **2013**, 1-10 (2013).
36. C. di Lauro, in *Rotational Structure in Molecular Infrared Spectra*. (Elsevier, 2013), chap. 10, pp. 225-245.
37. D. E. Weeks, W. G. Harter, Rotation Vibration Scalar Coupling Zeta Coefficients and Spectroscopic Band Shapes of Buckminsterfullerene. *Chem. Phys. Lett.* **176**, 209-216 (1991).
38. P. R. Bunker, P. Jensen, Spherical top molecules and the molecular symmetry group. *Mol. Phys.* **97**, 255-264 (1999).
39. T. C. Reimer, W. G. Harter, Fullerene symmetry reduction and rotational level fine structure: The buckyball isotopomer $^{12}\text{C}_{59}^{13}\text{C}$. *J. Chem. Phys.* **106**, 1326-1335 (1997).
40. W. G. Harter, D. E. Weeks, Rotation-Vibration Spectra of Icosahedral Molecules. I. Icosahedral Symmetry Analysis and Fine Structure. *J. Chem. Phys.* **90**, 4727-4743 (1989).
41. V. Boudon, J.-P. Champion, T. Gabard, M. Loëte, F. Michelot, G. Pierre, M. Rotger, C. Wenger, M. Rey, Symmetry-adapted tensorial formalism to model rovibrational and rovibronic spectra of molecules pertaining to various point groups. *J. Mol. Spectrosc.* **228**, 620-634 (2004).
42. J. Tennyson, P. F. Bernath, L. R. Brown, A. Campargue, A. G. Csaszar, L. Daumont, R. R. Gamache, J. T. Hodges, O. V. Naumenko, O. L. Polyansky, L. S. Rothman, A. C. Vandaele, N. F. Zobov, A. R. Al Derzi, C. Fabri, A. Z. Fazliev, T. Furtenbacher, I. E. Gordon, L. Lodi, I. I. Mizus, IUPAC critical evaluation of the rotational-vibrational spectra of water vapor, Part III: Energy levels and transition wavenumbers for H_2^{16}O . *J. Quant. Spectrosc. Radiat. Transfer* **117**, 29-58 (2013).
43. W. B. Olson, A. G. Maki, W. J. Lafferty, Tables of N_2O Absorption Lines for the Calibration of Tunable Infrared Lasers from 522 cm^{-1} to 657 cm^{-1} and from 1115 cm^{-1} to 1340 cm^{-1} . *J. Phys. Chem. Ref. Data* **10**, 1065-1084 (1981).
44. C. Camy-Peyret, J.-M. Flaud, A. Mahmoudi, G. Guelachvili, J. W. C. Johns, Line Positions and Intensities in the ν_2 Band of D_2O Improved Pumped D_2O Laser Frequencies. *Int. J. Infrared Millimeter Waves* **6**, 199-233 (1985).

Acknowledgments: The authors thank Hans Green for technical advice during the design of the oven source and John Doyle for insightful discussions. **Funding:** This work was supported by AFOSR Grant No. FA9550-15-1-0111, the DARPA SCOUT Program, NIST, and NSF PHYS-1734006. M.L.W. is supported through an NRC Postdoctoral Fellowship; **Author contributions:** P.B.C., M.L.W., and J.Y. performed the experiment. K.F.L. and M.E.F. built the difference frequency generation-based comb. All authors contributed to the writing of this paper; **Competing**

interests: We declare no competing interests. **Data and materials availability:** All data is available in the main text or the supplementary materials.

Supplementary Materials:

Materials and Methods

Figure S1

Data S1

References (42-44)

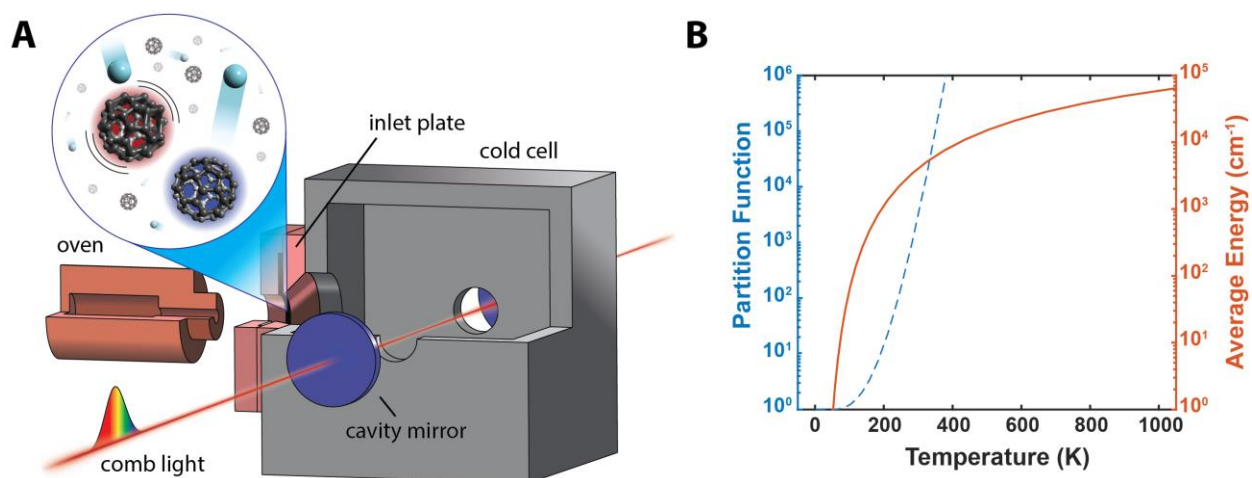


Fig. 1: Cooling and comb spectroscopy of gas-phase C₆₀. (A) Sublimated C₆₀ vapor exits the oven source and enters a cryogenic cell, where it thermalizes via collisions with cold buffer gas introduced through an annular slit inlet plate surrounding the entrance aperture (see inset). Mid-infrared frequency comb light is coupled to an optical enhancement cavity surrounding the cell. The optical absorption spectrum is measured with a scanning arm Fourier transform spectrometer (not pictured). (B) The vibrational partition function (blue dashed line) and average vibrational energy (red solid line) increase strongly as a function of temperature. Approximately 6-8 eV of vibrational energy must be removed per molecule to cool C₆₀ from the initial oven temperature to below 150 K, at which point the vibrational partition function is approximately equal to unity.

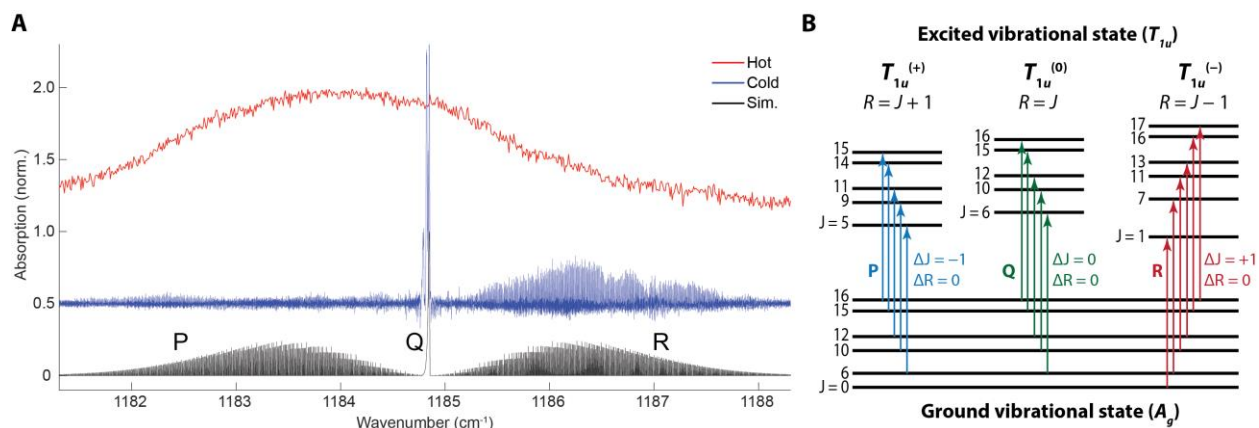


Fig. 2: Spectroscopic patterns of the IR active vibrational band of $^{12}\text{C}_{60}$ near $8.5\ \mu\text{m}$. (A) A simulated spectrum (bottom, black) is compared to a measured spectrum of cold (middle, blue) and hot (top, red) C_{60} . The measured hot spectrum shows broad, unresolved absorption due to many thermally occupied vibrational states. The cold spectrum exhibits sharp, well resolved rotational structure from transitions out of the ground vibrational state. (B) Rovibrational transitions between the ground vibrational state and the excited state follow zeroth order selection rules of $\Delta J = 0, \pm 1$ and $\Delta R = 0$. These lead to independent P ($\Delta J = -1$), Q ($\Delta J = 0$) and R ($\Delta J = +1$) branches that access the upper state manifolds labeled $T_{1u}^{(+)}$ (for $R = J + 1$), $T_{1u}^{(0)}$ (for $R = J$), and $T_{1u}^{(-)}$ (for $R = J - 1$), respectively.

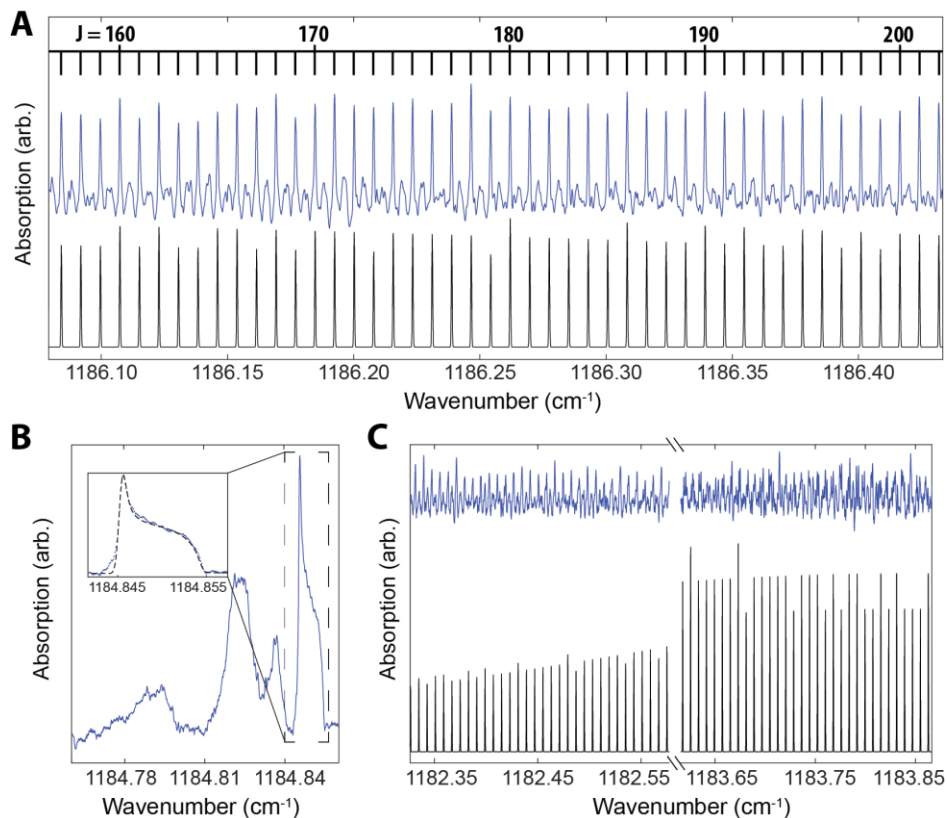


Fig. 3: Detailed views of portions of the measured IR band. (A) The R branch shows agreement between the expected intensity patterns from the simulation (bottom, black) and the measured spectrum (top, blue). The tie line above the spectrum indicates the lower state J value of each observed $R(J)$ transition. (B) The Q branch region of the spectrum contains several features. The highest wavenumber feature is assigned as the Q branch of the ¹²C₆₀ isotopologue. Inset: the dashed line represents a fit to a simple quartic centrifugal distortion contour. The additional features at lower frequencies are likely due to the singly substituted ¹³C¹²C₅₉ isotopologue. (C) These two portions of the P branch (top, blue) are representative of the disagreement with the zeroth order simulation determined from parameters fitted to the R branch (bottom, black). The structure not captured by the simulation is evidence of non-scalar centrifugal distortion effects.

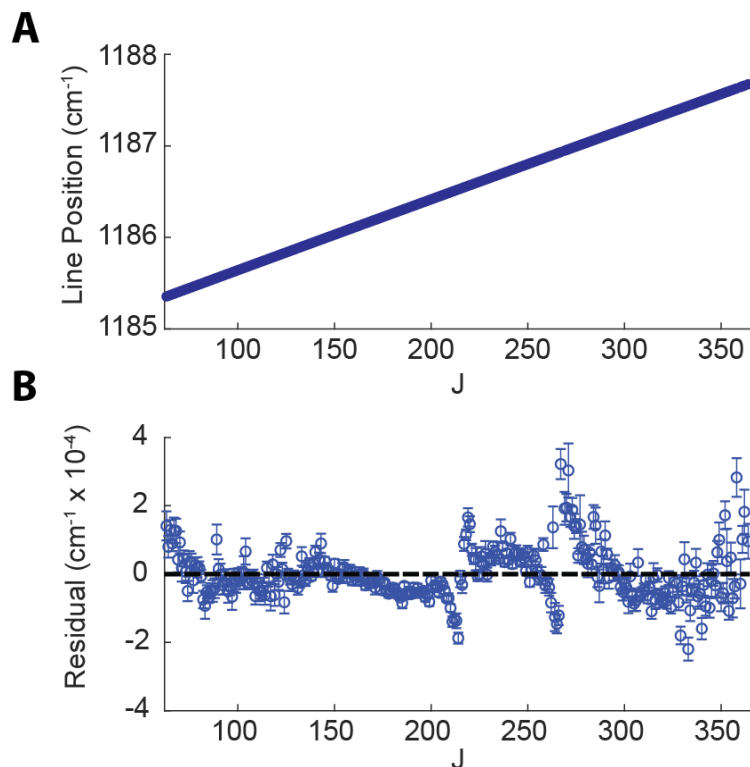


Fig. 4: Fit results for the R branch. (A) The $R(J)$ line positions plotted versus lower state J display a very linear trend over $J = 60$ -360. The individual line positions are listed in Data S1. (B) The residuals from the fit of Eq. (6) to these line positions, summarized in Table 1, exhibit apparent avoided crossings near $J = 215$ and $J = 275$, which are possible signatures of local dark state perturbers in the upper state.

Table 1: Fitted spectroscopic parameters of Eq. (6) for the R branch. The residuals (Fig. 4B) have a small root-mean-square error of $7.4 \times 10^{-5} \text{ cm}^{-1}$, slightly larger than the 1σ line-center measurement uncertainty of $2.5 \times 10^{-5} \text{ cm}^{-1}$.

Parameter	Value (cm⁻¹)
$\nu_0 + (2\bar{B} + \Delta B)(1 - 2\zeta)$	1184.86196(3)
$2\bar{B}(1 - \zeta) + \Delta B(2 - \zeta)$	0.0078300(3)
ΔB	$-2.876(6) \times 10^{-7}$

Supplementary Materials for

Quantum state resolution of the C₆₀ fullerene

P. Bryan Changala, Marissa L. Weichman, Kevin F. Lee, Martin E. Fermann, Jun Ye

Correspondence to: bryan.changala@colorado.edu (P.B.C.), ye@jila.colorado.edu (J.Y.)

This PDF file includes:

Materials and Methods

Fig. S1

Data S1

Materials and Methods

Experimental details

C_{60} is vaporized in a small cylindrical copper oven approximately 5 cm long and 3 cm in diameter, loaded with a few hundred milligrams of solid C_{60} powder (Fig. 1A, main text). The oven is heated to 950 K with two silicon nitride heaters clamped to the oven body. Gas exits the oven through a 3 mm hole at its end and enters an aluminum cold cell, $6 \times 6 \times 6 \text{ cm}^3$ in volume, anchored to a liquid nitrogen cold finger in vacuum. An annular slit buffer gas inlet plate surrounds the entrance aperture of the cold cell. At optimum conditions, a flow of 50-100 sccm of argon buffer gas is introduced into the cell through the annular inlet and the background chamber pressure is kept at 250 mTorr. The oven is placed 0.5 to 1.0 cm from the inlet aperture.

LWIR DFG comb light is generated with near-IR driving combs in an orientation patterned GaP crystal (31). The two driving fields originate from the same mode-locked erbium-doped fiber oscillator and therefore have an identical repetition rate $f_{\text{rep}} = 93.4 \text{ MHz}$ and carrier-envelope phase offset frequencies, f_0 . The resultant DFG light has comb teeth at frequencies equal to the difference of the two driving combs. Therefore, it has a passively stable $f_0 = 0$. We generate a non-zero DFG f_0 by inserting an acousto-optic modulator in one of the driving beam arms.

An absorption enhancement cavity is formed with two high reflectivity, low loss mirrors that surround the cell. They are spaced by 53.5 cm resulting in a cavity FSR of 280 MHz. Approximately 1 mW of comb light spanning $1150\text{-}1200 \text{ cm}^{-1}$ is resonantly coupled to the cavity. As the cavity $\text{FSR} = 3 \times f_{\text{rep}}$, only one out of every three comb modes is coupled into the cavity. Frequency sidebands are applied to the light at 2.65 MHz via an electro-optic modulator (EOM) in the oscillator cavity and are used to generate a Pound-Drever-Hall comb-cavity error signal. This error signal is filtered, amplified, and fed back to the EOM and to piezoelectric elements in the laser oscillator cavity to maintain the $\text{FSR} = 3 \times f_{\text{rep}}$ resonance condition. An oscillator monitor photodiode is used to measure the 11th harmonic of f_{rep} , which is phase-locked to a local oscillator by feeding back on enhancement cavity length piezos, simultaneously stabilizing the absolute values of f_{rep} and the cavity FSR.

When locked, 20-30% of the resonant comb mode power is transmitted through the cavity. The spectrum of the cavity transmission is measured with a scanning-arm Fourier transform interferometer (32,33). The LWIR interferogram is sampled at the zero-crossings of a $1 \text{ }\mu\text{m}$ cw-Nd:YAG NPRO laser that simultaneously propagates through the interferometer. Both output ports of the LWIR beam splitter are used to obtain a difference interferogram with an autobalanced circuit, suppressing common mode intensity noise. The instrument resolution of the interferometer (100 MHz) is sufficiently narrow to resolve individual comb teeth, spaced by the FSR of the cavity (280 MHz). We fill the FSR “gap” between cavity resonances by scanning the FSR and interleaving these spectra.

The cold spectrum plotted in blue in Fig 2A in the main text contains data averaged from 78 FSR scans, each consisting of 89 FSR positions evenly distributed over the 280 MHz span. This represents approximately 20 hours of total acquisition time

Frequency calibration and spectral fitting

A preliminary calibration of the optical frequencies is performed by exploiting absorption lines in the spectrum from trace H₂O inside the optical cavity. We first scale the nominal wavenumber axis from the interferometer trace for a given FSR to match known H₂O line positions in the 8.5 μm region (42). This provides sufficient accuracy to determine the integer mode index m of each comb tooth, which then determines the final absolute optical frequency via $\nu_m = m \times f_{\text{rep}} + f_0$. The values of f_{rep} and f_0 are ultimately locked to an atomic time standard with a relative frequency offset error below 10^{-12} . The absolute frequencies were verified by checking the recalibrated trace H₂O line positions, as well as N₂O and D₂O line positions obtained in separate measurements. All were consistent with reference literature values (42-44).

The R branch transitions were fit to Gaussian profiles to determine the linewidth, intensity, and center position of each transition. These parameters are summarized in Data S1. An example fit of the R(180) transition is shown in Fig. S1A. The absolute line center measurement uncertainty is $2.5 \times 10^{-5} \text{ cm}^{-1}$, dominated by the statistical uncertainty given by our measurement signal-to-noise and the absorption line widths, which range from $0.5 \times 10^{-3} \text{ cm}^{-1}$ to $1.0 \times 10^{-3} \text{ cm}^{-1}$. The intensities of the R branch transitions permit extraction of the relative rotational populations in the ground vibrational state, which display a Boltzmann distribution with an effective rotational temperature $T_{\text{rot}} = 150(2) \text{ K}$ (Fig. S1B).

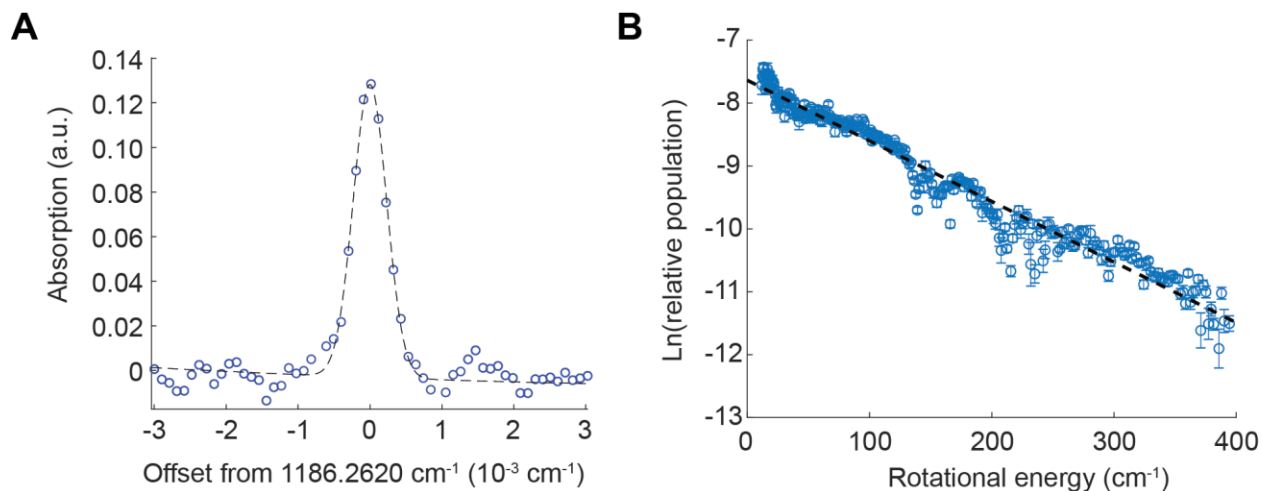


Fig. S1. Absorption line shape and temperature fits. (A) The absorption line assigned to the R(180) transition (blue circles) is fitted to a Gaussian profile (black dashed line) with center position $1186.261999(8) \text{ cm}^{-1}$ and full-width-at-half-maximum (FWHM) of $16.0(6) \text{ MHz}$. (B) The natural logarithms of the relative ground state rotational level populations (blue circles) are plotted against the ground state rotational energy. The linear trend indicates a Boltzmann distribution with rotational temperature $T_{\text{rot}} = 150(2) \text{ K}$ (black dashed line).

Data S1 (separate file). Fitted parameters for individual R branch transitions. This table summarizes the least-squares fitted line center frequency, full-width-at-half-maximum (FWHM), and relative intensity of R(J) transitions for $J = 63\text{-}364$. The mean line center uncertainty is $2.5 \times 10^{-5} \text{ cm}^{-1}$.

Data S1. Fitted parameters for individual R branch transitions. This table summarizes the least-squares fitted line center frequency, full-width-at-half-maximum (FWHM), and relative intensity of R(J) transitions for J = 63-364. The mean line center uncertainty is $2.5 \times 10^{-5} \text{ cm}^{-1}$.

Branch	J	Fitted Line		FWHM		Intensity		Comment
		Center (cm^{-1})	Uncertainty	(MHz)	Unc.	(a.u)	Unc.	
R	63	1185.35424585	0.00004268	19.14	2.95	0.0288	0.0043	
R	64	1185.36197804	0.00003169	22.82	2.24	0.0334	0.0028	
R	65	1185.36982044	0.00002900	21.28	2.05	0.0384	0.0032	
R	66	1185.37757323	0.00002253	21.07	1.59	0.0519	0.0034	
R	67	1185.38540278	0.00003757	33.99	2.65	0.0407	0.0027	
R	68	1185.39319309	0.00003552	19.95	2.51	0.0339	0.0037	
R	69	1185.40089960	0.00003726	20.68	2.42	0.0342	0.0037	
R	70	1185.40873990	0.00003218	23.04	2.27	0.0448	0.0038	
R	71	1185.41645406	0.00003947	29.48	2.79	0.0386	0.0032	
R	72	1185.42427124	0.00002310	22.95	1.63	0.0565	0.0035	
R	73	1185.43202051	0.00003286	12.98	2.32	0.0368	0.0057	
R	74	1185.43975187	0.00002988	19.43	2.11	0.0435	0.0041	
R	75	1185.44762428	0.00003147	25.20	2.10	0.0490	0.0037	
R	76	1185.45540796	0.00002710	25.16	1.91	0.0503	0.0033	
R	77	1185.46314285	0.00003698	24.06	2.61	0.0400	0.0038	
R	78	1185.47097227	0.00002255	20.29	1.59	0.0624	0.0042	
R	79	1185.47875112	0.00002965	19.23	2.09	0.0402	0.0038	
R	80	1185.48653437	0.00001873	20.91	1.32	0.0583	0.0032	
R	81	1185.49429358	0.00001909	21.74	1.27	0.0582	0.0029	
R	82	1185.50200781	0.00002540	29.02	1.79	0.0600	0.0032	
R	83	1185.50977212	0.00003768	28.19	2.66	0.0406	0.0033	
R	84	1185.51759455	0.00001952	19.92	1.38	0.0584	0.0035	
R	85	1185.52536049	0.00001683	20.12	1.19	0.0598	0.0031	
R	86	1185.53315998	0.00002239	22.89	1.58	0.0546	0.0033	
R	87	1185.54094013	0.00003179	28.74	2.14	0.0518	0.0033	
R	88	1185.54872794	0.00002867	27.97	2.02	0.0436	0.0027	
R	89	1185.55664970	0.00004396	29.24	3.10	0.0284	0.0026	
R	90	1185.56434195	0.00002859	18.73	2.02	0.0652	0.0061	
R	91	1185.57210311	0.00003231	25.00	2.28	0.0530	0.0042	
R	92	1185.57985054	0.00002848	25.09	2.01	0.0564	0.0039	
R	93	1185.58763468	0.00003497	29.44	2.39	0.0512	0.0035	
R	94	1185.59541831	0.00003099	24.71	2.19	0.0489	0.0037	
R	95	1185.60315991	0.00003314	30.45	2.34	0.0541	0.0036	
R	96	1185.61094782	0.00002324	31.04	1.64	0.0736	0.0034	
R	97	1185.61869410	0.00003831	30.82	2.70	0.0470	0.0036	
R	98	1185.62651645	0.00003343	21.25	2.36	0.0482	0.0046	
R	99	1185.63428416	0.00003167	30.41	2.22	0.0513	0.0031	
R	100	1185.64207236	0.00002515	26.03	1.78	0.0680	0.0040	
R	101	1185.64983920	0.00003020	21.19	2.13	0.0416	0.0036	
R	102	1185.65762641	0.00001848	18.85	1.30	0.0747	0.0045	
R	103	1185.66539970	0.00004810	38.65	3.40	0.0579	0.0044	

R 104	1185.67323207	0.00003855	31.42	2.76	0.0547	0.0041
R 105	1185.68090914	0.00001679	23.63	1.22	0.0791	0.0034
R 106	1185.68867766	0.00001698	20.58	1.20	0.0792	0.0040
R 107	1185.69645552	0.00002512	31.35	1.77	0.0638	0.0031
R 108	1185.70423612	0.00001867	13.90	1.32	0.0655	0.0054
R 109	1185.71194481	0.00002460	16.39	1.74	0.0565	0.0052
R 110	1185.71975049	0.00002559	20.56	1.82	0.0790	0.0060
R 111	1185.72749293	0.00002915	17.69	2.06	0.0681	0.0069
R 112	1185.73525949	0.00002280	17.00	1.61	0.0642	0.0053
R 113	1185.74303598	0.00002731	32.10	1.93	0.0592	0.0031
R 114	1185.75077680	0.00002752	29.95	1.94	0.0762	0.0043
R 115	1185.75862079	0.00001891	22.01	1.34	0.0726	0.0038
R 116	1185.76635157	0.00002079	17.36	1.49	0.0676	0.0050
R 117	1185.77406457	0.00004171	34.35	2.99	0.0652	0.0048
R 118	1185.78192048	0.00002797	22.66	1.97	0.0651	0.0049
R 119	1185.78959260	0.00003175	15.78	2.24	0.0449	0.0055
R 120	1185.79741540	0.00002041	22.30	1.44	0.0879	0.0049
R 121	1185.80515325	0.00002416	25.18	1.71	0.0721	0.0042
R 122	1185.81300636	0.00002014	26.29	1.42	0.0708	0.0031
R 123	1185.82071021	0.00001860	19.63	1.31	0.0700	0.0041
R 124	1185.82837197	0.00003296	34.45	2.33	0.0715	0.0042
R 125	1185.83630935	0.00002124	25.91	1.50	0.0833	0.0042
R 126	1185.84397063	0.00001532	14.80	1.08	0.0832	0.0053
R 127	1185.85171409	0.00001655	15.13	1.17	0.0693	0.0046
R 128	1185.85945447	0.00001980	19.44	1.28	0.0776	0.0046
R 129	1185.86723090	0.00002003	21.30	1.41	0.0720	0.0041
R 130	1185.87499018	0.00001291	16.93	0.91	0.0914	0.0043
R 131	1185.88271027	0.00001954	15.77	1.38	0.0783	0.0059
R 132	1185.89048580	0.00002045	27.89	1.44	0.1051	0.0047
R 133	1185.89831131	0.00002719	26.00	1.92	0.0740	0.0047
R 134	1185.90600900	0.00002439	18.55	1.86	0.0730	0.0072
R 135	1185.91374619	0.00001616	18.83	1.14	0.0904	0.0047
R 136	1185.92153041	0.00001960	26.21	1.38	0.0956	0.0044
R 137	1185.92929557	0.00001914	17.19	1.35	0.0756	0.0051
R 138	1185.93701210	0.00001066	16.48	0.75	0.0984	0.0039
R 139	1185.94480059	0.00001620	18.37	1.14	0.0851	0.0046
R 140	1185.95258422	0.00001861	21.19	1.26	0.1052	0.0059
R 141	1185.96027741	0.00001746	18.45	1.23	0.0899	0.0052
R 142	1185.96805973	0.00002046	25.56	1.44	0.1016	0.0050
R 143	1185.97585529	0.00002827	19.90	2.00	0.0727	0.0063
R 144	1185.98351867	0.00001217	14.50	0.86	0.1018	0.0052
R 145	1185.99129801	0.00001223	16.65	0.86	0.0989	0.0044
R 146	1185.99902453	0.00001259	16.01	0.92	0.1100	0.0053
R 147	1186.00676011	0.00001487	17.50	1.05	0.1006	0.0052
R 148	1186.01449179	0.00001136	15.68	0.80	0.1002	0.0044
R 149	1186.02220786	0.00001804	24.40	1.27	0.0987	0.0045
R 150	1186.03001614	0.00001360	25.10	0.96	0.1262	0.0042

R 151	1186.03772855	0.00001409	20.62	1.00	0.0978	0.0041
R 152	1186.04545773	0.00001200	20.61	0.85	0.0981	0.0035
R 153	1186.05321004	0.00001675	22.09	1.18	0.0973	0.0045
R 154	1186.06097027	0.00001853	19.54	1.31	0.1014	0.0059
R 155	1186.06871718	0.00002094	16.79	1.48	0.0829	0.0063
R 156	1186.07642558	0.00001295	16.95	0.91	0.1148	0.0054
R 157	1186.08418307	0.00001604	21.55	1.17	0.1015	0.0045
R 158	1186.09192937	0.00001537	22.66	1.09	0.0998	0.0041
R 159	1186.09963778	0.00001438	19.65	1.02	0.0982	0.0044
R 160	1186.10738918	0.00001095	18.62	0.77	0.1240	0.0045
R 161	1186.11513853	0.00001351	19.21	0.95	0.0964	0.0041
R 162	1186.12284990	0.00001509	17.86	1.07	0.1197	0.0062
R 163	1186.13060482	0.00002077	19.44	1.34	0.0959	0.0060
R 164	1186.13832988	0.00001974	17.53	1.39	0.0935	0.0064
R 165	1186.14607679	0.00001656	17.79	1.17	0.1056	0.0060
R 166	1186.15377851	0.00001322	19.09	0.93	0.1178	0.0050
R 167	1186.16152842	0.00001645	22.74	1.16	0.1072	0.0047
R 168	1186.16925271	0.00001354	19.67	0.96	0.1257	0.0053
R 169	1186.17698789	0.00001497	21.33	1.02	0.1025	0.0046
R 170	1186.18472034	0.00001352	19.87	0.95	0.1148	0.0048
R 171	1186.19243731	0.00001968	21.83	1.39	0.1216	0.0067
R 172	1186.20020052	0.00001716	14.42	1.21	0.1203	0.0088
R 173	1186.20792414	0.00001046	16.67	0.74	0.1132	0.0043
R 174	1186.21562235	0.00001038	16.69	0.73	0.1222	0.0046
R 175	1186.22337610	0.00001185	17.74	0.87	0.1230	0.0050
R 176	1186.23110229	0.00000911	15.85	0.64	0.1137	0.0040
R 177	1186.23880472	0.00000990	16.71	0.70	0.1221	0.0044
R 178	1186.24652716	0.00001232	20.67	0.87	0.1395	0.0051
R 179	1186.25426457	0.00001249	17.60	0.88	0.1110	0.0048
R 180	1186.26199875	0.00000803	15.99	0.57	0.1299	0.0040
R 181	1186.26972423	0.00000980	16.54	0.69	0.1172	0.0042
R 182	1186.27743638	0.00001181	17.88	0.83	0.1104	0.0045
R 183	1186.28515380	0.00000985	15.40	0.70	0.1162	0.0045
R 184	1186.29287109	0.00000827	15.34	0.58	0.1216	0.0040
R 185	1186.30057909	0.00001579	18.56	1.11	0.1023	0.0053
R 186	1186.30835263	0.00001044	19.50	0.71	0.1353	0.0040
R 187	1186.31605358	0.00001004	17.41	0.71	0.1137	0.0040
R 188	1186.32377260	0.00001370	16.69	0.97	0.1114	0.0056
R 189	1186.33150299	0.00001384	15.98	0.98	0.1140	0.0060
R 190	1186.33921676	0.00001113	19.32	0.79	0.1337	0.0047
R 191	1186.34695558	0.00001377	14.67	0.97	0.1093	0.0063
R 192	1186.35465968	0.00001314	15.03	0.85	0.1272	0.0070
R 193	1186.36239364	0.00001202	16.49	0.85	0.1100	0.0049
R 194	1186.37009762	0.00001119	15.66	0.79	0.1035	0.0045
R 195	1186.37782009	0.00001053	16.00	0.74	0.1300	0.0052
R 196	1186.38553942	0.00000959	16.52	0.68	0.1297	0.0046
R 197	1186.39323692	0.00001149	16.21	0.81	0.1046	0.0045

R 198	1186.40096105	0.00000907	15.41	0.65	0.1207	0.0043
R 199	1186.40865637	0.00001236	15.75	0.87	0.0985	0.0047
R 200	1186.41643408	0.00001252	16.38	0.88	0.1122	0.0052
R 201	1186.42412871	0.00000721	17.12	0.51	0.1320	0.0034
R 202	1186.43185019	0.00001113	16.87	0.79	0.1214	0.0049
R 203	1186.43955701	0.00001257	16.23	0.89	0.1015	0.0048
R 204	1186.44725348	0.00001081	16.42	0.76	0.1134	0.0046
R 205	1186.45499854	0.00001037	16.80	0.73	0.1081	0.0041
R 206	1186.46270031	0.00000935	15.74	0.66	0.1186	0.0043
R 207	1186.47039538	0.00001012	16.15	0.71	0.1092	0.0042
R 208	1186.47808243	0.00000841	16.50	0.59	0.1169	0.0036
R 209	1186.48579442	0.00001380	18.90	0.95	0.0865	0.0042
R 210	1186.49347467	0.00001148	16.06	0.81	0.1140	0.0050
R 211	1186.50114337	0.00001520	18.00	1.07	0.0936	0.0048
R 212	1186.50885975	0.00001096	19.73	0.77	0.0973	0.0033
R 213	1186.51656248	0.00002158	25.22	1.52	0.0802	0.0042
R 214	1186.52421866	0.00001630	21.29	1.15	0.0736	0.0034
R 215	1186.53209836	0.00002436	30.00	1.64	0.0595	0.0029
R 216	1186.53978741	0.00002455	30.19	1.73	0.0532	0.0026
R 217	1186.54761244	0.00002038	24.25	1.44	0.0652	0.0034
R 218	1186.55534459	0.00001570	21.39	1.11	0.0774	0.0035
R 219	1186.56309952	0.00002686	32.36	1.90	0.0784	0.0040
R 220	1186.57078332	0.00002312	15.03	1.63	0.0783	0.0074
R 221	1186.57841159	0.00001755	14.30	1.24	0.0965	0.0072
R 222	1186.58608865	0.00001642	14.68	1.16	0.0970	0.0066
R 223	1186.59378887	0.00003248	18.51	2.29	0.0825	0.0089
R 224	1186.60144044	0.00001420	16.95	1.00	0.0872	0.0045
R 225	1186.60914619	0.00001355	18.13	0.96	0.0839	0.0038
R 226	1186.61689892	0.00002758	17.82	1.91	0.0736	0.0063
R 227	1186.62457604	0.00002413	18.86	1.70	0.0645	0.0050
R 228	1186.63230577	0.00003746	32.39	2.64	0.0630	0.0045
R 229	1186.63994363	0.00002034	23.59	1.44	0.0633	0.0033
R 230	1186.64768754	0.00001782	16.47	1.26	0.0723	0.0048
R 231	1186.65538176	0.00001598	17.90	1.13	0.0724	0.0040
R 232	1186.66311862	0.00001496	17.33	0.96	0.0812	0.0040
R 233	1186.67079875	0.00001785	19.94	1.26	0.0741	0.0041
R 234	1186.67848280	0.00001506	16.53	1.06	0.0827	0.0046
R 235	1186.68616832	0.00001294	14.66	0.91	0.0851	0.0046
R 236	1186.69394465	0.00003491	33.84	2.46	0.0466	0.0029
R 237	1186.70159502	0.00001226	15.75	0.87	0.0956	0.0046
R 238	1186.70924145	0.00001290	12.92	0.91	0.0809	0.0049
R 239	1186.71696012	0.00001211	14.38	0.85	0.0782	0.0040
R 240	1186.72463295	0.00001143	16.40	0.81	0.1059	0.0045
R 241	1186.73238632	0.00001766	22.72	1.25	0.1001	0.0048
R 242	1186.74000359	0.00001206	17.05	0.85	0.0954	0.0041
R 243	1186.74772460	0.00002134	18.50	1.39	0.0943	0.0061
R 244	1186.75542004	0.00001936	16.52	1.37	0.0868	0.0062

R 245	1186.76310495	0.00001528	19.08	1.08	0.0929	0.0045
R 246	1186.77076898	0.00001103	17.70	0.78	0.1045	0.0040
R 247	1186.77847906	0.00001635	20.04	1.15	0.0892	0.0044
R 248	1186.78615560	0.00001735	15.16	1.23	0.0761	0.0053
R 249	1186.79380480	0.00001213	16.31	0.90	0.0941	0.0042
R 250	1186.80154745	0.00001827	21.70	1.29	0.0943	0.0049
R 251	1186.80914515	0.00001403	18.48	0.99	0.0682	0.0032
R 252	1186.81686652	0.00001005	16.21	0.71	0.0918	0.0035
R 253	1186.82459259	0.00001745	20.98	1.23	0.0837	0.0043
R 254	1186.83226351	0.00003358	15.25	2.38	0.0599	0.0081
R 255	1186.83991344	0.00001913	13.86	1.35	0.0799	0.0067
R 256	1186.84757925	0.00001986	16.62	1.40	0.0757	0.0055
R 257	1186.85526730	0.00002549	19.24	1.80	0.0647	0.0052
R 258	1186.86304021	0.00001858	17.50	1.31	0.0685	0.0044
R 259	1186.87060153	0.00002146	21.13	1.52	0.0599	0.0037
R 260	1186.87829548	0.00002413	18.29	1.75	0.0638	0.0059
R 261	1186.88595696	0.00002378	15.11	1.68	0.0588	0.0057
R 262	1186.89359208	0.00002823	20.25	1.99	0.0676	0.0058
R 263	1186.90149148	0.00006144	28.72	4.34	0.0415	0.0054
R 264	1186.90890727	0.00004101	12.46	2.89	0.0385	0.0077
R 265	1186.91656494	0.00002762	32.01	1.99	0.0475	0.0025
R 266	1186.92426711	0.00002823	31.80	2.04	0.0559	0.0030
R 267	1186.93238705	0.00004437	48.22	3.13	0.0400	0.0023
R 268						
R 269	1186.94760886	0.00004808	33.84	3.39	0.0250	0.0022
R 270	1186.95528590	0.00004018	40.23	2.84	0.0530	0.0032
R 271	1186.96306953	0.00007914	30.95	5.53	0.0594	0.0089
R 272	1186.97060737	0.00002971	18.22	2.10	0.0666	0.0066
R 273	1186.97830157	0.00003481	29.55	2.46	0.0752	0.0054
R 274	1186.98592563	0.00003686	16.47	2.60	0.0556	0.0076
R 275	1186.99359848	0.00002016	13.96	1.42	0.0619	0.0055
R 276	1187.00118385	0.00002134	21.08	1.51	0.0753	0.0047
R 277	1187.00894545	0.00008556	49.30	5.99	0.0695	0.0076
R 278	1187.01654953	0.00004536	17.29	3.20	0.0448	0.0072
R 279	1187.02421175	0.00004149	7.28	2.91	0.0326	0.0113
R 280	1187.03185535	0.00001606	15.82	1.13	0.0691	0.0043
R 281	1187.03950923	0.00003973	16.80	2.80	0.0282	0.0041
R 282	1187.04720940	0.00002218	12.71	1.57	0.0577	0.0062
R 283	1187.05484296	0.00002845	30.25	2.01	0.0625	0.0036
R 284	1187.06264838	0.00003455	35.25	2.44	0.0559	0.0033
R 285	1187.07028938	0.00005310	17.58	3.75	0.0391	0.0072
R 286	1187.07780484	0.00002974	13.18	2.10	0.0467	0.0064
R 287	1187.08544396	0.00004831	23.86	3.41	0.0625	0.0077
R 288	1187.09320928	0.00003574	20.44	2.35	0.0708	0.0074
R 289	1187.10082022	0.00004011	25.64	2.83	0.0559	0.0053
R 290	1187.10858367	0.00004108	27.66	2.90	0.0635	0.0058
R 291	1187.11619249	0.00001530	16.74	1.08	0.0616	0.0034

Line obscured, not fitted.

R 292	1187.12378493	0.00003189	13.28	2.25	0.0462	0.0068
R 293	1187.13147483	0.00001438	19.29	1.03	0.0435	0.0020
R 294	1187.13913088	0.00003070	28.68	2.18	0.0642	0.0042
R 295	1187.14680545	0.00002984	19.92	2.11	0.0536	0.0049
R 296	1187.15444326	0.00002383	21.81	1.68	0.0575	0.0038
R 297	1187.16210434	0.00002018	25.17	1.42	0.0679	0.0033
R 298	1187.16972032	0.00002087	19.59	1.47	0.0550	0.0036
R 299	1187.17736489	0.00002570	18.33	1.67	0.0467	0.0039
R 300	1187.18504860	0.00002107	20.06	1.49	0.0577	0.0037
R 301	1187.19269127	0.00002980	17.72	2.10	0.0616	0.0063
R 302	1187.20030655	0.00003323	22.76	2.35	0.0644	0.0057
R 303	1187.20803730	0.00003697	32.37	2.61	0.0673	0.0047
R 304	1187.21563514	0.00002219	17.64	1.58	0.0670	0.0052
R 305	1187.22326750	0.00002150	20.11	1.52	0.0578	0.0038
R 306	1187.23093070	0.00003052	22.58	2.15	0.0525	0.0043
R 307	1187.23869592	0.00003952	19.63	2.79	0.0652	0.0080
R 308	1187.24625073	0.00001617	13.64	1.14	0.0541	0.0039
R 309	1187.25391044	0.00001833	20.01	1.29	0.0579	0.0032
R 310	1187.26157453	0.00001790	17.54	1.20	0.0600	0.0039
R 311	1187.26925509	0.00001644	19.31	1.16	0.0500	0.0026
R 312	1187.27685924	0.00002335	17.11	1.65	0.0479	0.0040
R 313	1187.28453206	0.00001863	16.24	1.32	0.0548	0.0038
R 314	1187.29211286	0.00002159	15.16	1.52	0.0460	0.0040
R 315	1187.29985955	0.00004309	30.51	3.11	0.0374	0.0032
R 316	1187.30744477	0.00002762	21.00	1.95	0.0473	0.0038
R 317	1187.31516486	0.00001950	17.28	1.38	0.0495	0.0034
R 318	1187.32275327	0.00001871	19.04	1.32	0.0554	0.0033
R 319	1187.33038469	0.00002145	22.64	1.51	0.0610	0.0035
R 320	1187.33803062	0.00001961	23.00	1.38	0.0594	0.0031
R 321	1187.34569783	0.00001991	21.02	1.35	0.0556	0.0033
R 322	1187.35332058	0.00002365	22.28	1.67	0.0528	0.0034
R 323	1187.36103138	0.00002012	22.58	1.42	0.0495	0.0027
R 324	1187.36859051	0.00001867	25.08	1.32	0.0629	0.0029
R 325	1187.37627897	0.00001760	22.10	1.24	0.0505	0.0025
R 326	1187.38395213	0.00001768	21.32	1.27	0.0619	0.0031
R 327	1187.39158828	0.00002449	32.09	1.75	0.0523	0.0024
R 328	1187.39917407	0.00002288	29.47	1.62	0.0477	0.0023
R 329	1187.40671845	0.00002574	32.80	1.82	0.0439	0.0021
R 330	1187.41450257	0.00002633	22.77	1.86	0.0373	0.0026
R 331	1187.42222185	0.00004998	33.76	3.53	0.0471	0.0043
R 332	1187.42977001	0.00003534	46.50	2.50	0.0503	0.0024
R 333	1187.43723706	0.00003374	39.93	2.38	0.0425	0.0022
R 334	1187.44498861	0.00003096	28.04	2.19	0.0396	0.0027
R 335	1187.45268561	0.00001893	15.49	1.34	0.0389	0.0029
R 336	1187.46034441	0.00003508	31.17	2.48	0.0457	0.0031
R 337	1187.46803953	0.00003990	28.80	2.87	0.0387	0.0032
R 338	1187.47557636	0.00003613	28.43	2.55	0.0387	0.0030

R 339	1187.48322006	0.00003718	26.63	2.62	0.0370	0.0032	
R 340	1187.49075223	0.00003124	29.17	2.21	0.0400	0.0026	
R 341	1187.49851448	0.00003157	29.95	2.23	0.0409	0.0026	
R 342	1187.50608509	0.00002714	33.49	1.92	0.0448	0.0022	
R 343	1187.51381102	0.00003351	30.42	2.26	0.0391	0.0026	
R 344	1187.52134618	0.00002902	33.28	2.05	0.0389	0.0021	
R 345	1187.52905720	0.00004661	32.70	3.29	0.0336	0.0029	
R 346	1187.53671010	0.00003633	22.03	2.57	0.0347	0.0035	
R 347	1187.54430594	0.00003621	24.19	2.56	0.0265	0.0024	
R 348	1187.55203277	0.00003358	37.63	2.29	0.0470	0.0025	
R 349	1187.55969876	0.00005066	28.27	3.58	0.0272	0.0030	
R 350	1187.56715958	0.00004077	29.04	2.88	0.0349	0.0030	
R 351	1187.57480010	0.00003001	24.45	2.12	0.0360	0.0027	
R 352	1187.58265594	0.00004076	38.48	2.88	0.0433	0.0028	
R 353	1187.59014902	0.00009490	20.78	6.70	0.0176	0.0049	
R 354	1187.59763021	0.00002611	20.40	1.87	0.0396	0.0031	
R 355	1187.60541239	0.00004333	28.31	3.06	0.0356	0.0033	
R 356	1187.61291834	0.00005625	14.07	3.97	0.0215	0.0053	
R 357	1187.62057818	0.00003542	19.59	2.50	0.0273	0.0030	
R 358	1187.62852169	0.00005657	36.80	3.99	0.0215	0.0020	
R 359							Line obscured, not fitted.
R 360	1187.64345718	0.00007134	14.23	5.04	0.0159	0.0049	
R 361	1187.65120987	0.00003946	26.06	2.79	0.0355	0.0033	
R 362	1187.65891274	0.00006469	21.68	4.57	0.0229	0.0042	
R 363							Line obscured, not fitted.
R 364	1187.67406893	0.00005100	25.67	3.62	0.0221	0.0027	